IEEE Access
Multidisciplinary | Rapid Review | Open Access Journal

Received January 21, 2018, accepted March 19, 2018, date of publication March 23, 2018, date of current version April 23, 2018.

Digital Object Identifier 10.1109/ACCESS.2018.2818741

Land Surface Temperature Retrieval From Landsat-8 Data With the Generalized Split-Window Algorithm

SHANSHAN LI AND GENG-MING JIANG, (Member, IEEE)

Key Laboratory for Information Science of Electromagnetic Waves (Ministry of Education), Fudan University, Shanghai 200433, China

Corresponding author: Geng-Ming Jiang (jianggm@fudan.edu.cn).

This work was supported in part by the National Key Research and Development Program of China from Ministry of Science and Technology, China, under Grant 2016YFB0501504, and in part by the National Natural Science Foundation of China under Grant 41271012 and Grant 40901158.

ABSTRACT This paper addresses land surface temperature (LST) retrieval from Landsat-8 data using the generalized split-window (GSW) algorithm. First, radiative transfer modeling experiment is conducted using the moderate spectral resolution atmospheric transmittance algorithm and computer model fed with SeeBor V5.0 atmospheric profile database to build a data set of LST related to brightness temperatures in Thermal Infrared Sensor (TIRS) bands 10 and 11, land surface emissivities (LSEs), and total precipitable water (TPW). Then, the GSW algorithm's coefficients are obtained through linear regression, in which the simulated data are grouped into several sub-ranges to improve the accuracy. The impacts of noise equivalent temperature difference and uncertainty of LSEs and TPW on derived LST are evaluated. Next, the TIRS channels 10 and 11 are inter-calibrated against the channels of infrared atmospheric sounding interferometer on board Metop-B. After that, LST is retrieved from the re-calibrated and clear sky Landsat-8 data using the GSW algorithm, where LSEs are estimated from the measurements of operational land imager on Landsat-8 by the modified normalized difference vegetation index (NDVI) based emissivity method, and TPW is extracted from the european centre for medium-range weather forecasts reanalysis data. Finally, the retrieved LST is cross-validated with the MOD11_L2 V6 product. The results show that the GSW algorithm can accurately retrieve LST from Landsat-8 data, and errors mainly come from the uncertainty of LSEs and TPW. Against the MOD11_L2 V6 product, the LST errors are -1.45 ± 0.80 K and -0.49 ± 0.78 K before and after the correction of LSEs and TPW, respectively.

INDEX TERMS Algorithm, infrared sensors, land surface temperature.

I. INTRODUCTION

Land surface temperature (LST) is a key parameter in the physics of land surface processes on regional as well as a global scale, combining the results of all surface–atmosphere interactions and energy fluxes between the atmosphere and the ground [1]. It is critical to have access to accurate estimates of LST because many applications in climatological, hydrological, ecological, and biogeochemical studies rely on the knowledge of LST [2]–[4]. In order to accurately retrieve LST, many algorithms have been developed, and they can be roughly grouped into three categories: the single-channel algorithm [5], [6], multi-channel algorithm [7]–[13], and multi-angle algorithm [14]. The commonly used multi-channel method is the split-window algorithm, which takes the advantage of atmospheric water vapor absorption difference between two channels respectively centered at around 11.0 μm and around 12 μm to eliminate the influence of atmosphere [7].

In the past decades, a series of instruments with split-window channels have been sent into space, such as the Advanced Very High Resolution Radiometer (AVHRR) on series of National Oceanic and Atmospheric Administration (NOAA) satellites, the Moderate-resolution Imaging Spectroradiometer (MODIS) aboard Terra and Aqua, the Visible and Infrared Radiometer (VIRR) on board Chinese Fengyun 3 satellites, and so on. Landsat-8, the eighth satellite in the Landsat program, was successfully launched into space on February 11, 2013. It carries two instruments, the Land

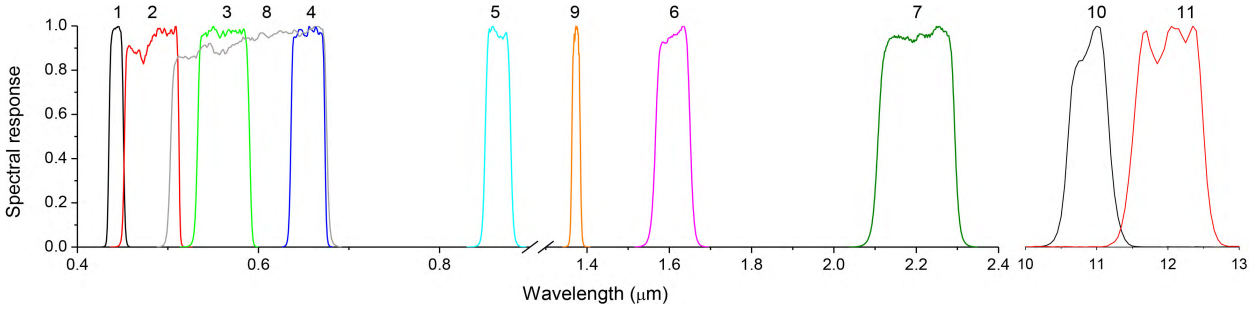

FIGURE 1. Spectral response functions of OLI and TIRS channels.

TABLE 1. Technical specification of operational land imager (OLI) on Landsat-8.

Band Name	Spectral range (μm)	Spatial resolution (m)
Band 1 (Coastal)	0.43 – 0.45	30
Band 2 (Blue)	0.45 – 0.51	30
Band 3 (Green)	0.53 – 0.59	30
Band 4 (Red)	0.64 – 0.67	30
Band 5 (NIR)	0.85 – 0.88	30
Band 6 (SWIR 1)	1.57 – 1.65	30
Band 7 (SWIR 2)	2.11 – 2.29	30
Band 8 (Pan)	0.50 – 0.68	15
Band 9 (Cirrus)	1.36 – 1.38	30

TABLE 2. Technical specification of thermal infrared sensor (TIRS) on Landsat-8.

Band name	Central wavelength (μm)	Spectral range (μm)	Spatial resolution (m)	NEΔT[1] at 320 K (K)
Band 10	10.9	10.6~11.2	100	0.046
Band 11	12.0	11.5~12.5	100	0.049

[1] NEΔT: Noise Equivalent Temperature Difference

Imager (OLI) and the Thermal Infrared Sensor (TIRS) (https://landsat.usgs.gov). The OLI instrument includes nine refined heritage bands in visible, near-infrared (NIR) and short wave infrared (SWIR), along with three new bands: a deep blue for coastal/aerosol studies, a shortwave infrared band for cirrus detection, and a quality assessment band (Table 1), while the TIRS instrument has two thermal infrared bands respectively centered at 10.9 μm and 12.0 μm (Table 2). The two instruments on Landsat-8 are superior to the Thematic Mapper (TM) and Enhanced Thematic Mapper Plus (ETM+) aboard previous Landsat satellites. Figure 1 shows the Spectral Response Functions (SRFs) of both OLI and TIRS channels. Another advantage is that the OLI and TIRS instruments observe Earth's surfaces with moderate-resolution from 15 meters to 100 meters, which is higher than most of Low Earth Orbit (LEO) satellites. According to the technical specification, the Landsat-8 measurements are very suitable for LST mapping. Recently, single-channel algorithms [15], [16] and split-window algorithms [17]–[19] have been developed to retrieve LST from the Landsat-8 data. Previous research compared the performance between the single-channel algorithm and the split-window algorithm for Landsat-8 LST retrieval, and concluded that the split-window algorithm is much more accurate [18], [20]. The Generalized Split-Window (GSW) algorithm proposed by Wan and Dozier [9] has been widely used to retrieve LST from satellite measurements, such as the AVHRR, MODIS and VIRR data, and its performance is perfect. Therefore, the GSW algorithm will be developed with radiative transfer modeling experiment to retrieve LST from the Landsat-8 data in this work.

This paper is organized as follows: Section II describes the methodology of LST retrieval. Section III presents the data description and processing. Section IV demonstrates the application of LST retrieval from Landsat-8 data. Section V is devoted to the cross-validation and analysis, and Section VI is about the summary and conclusion.

II. METHODOLOGY

A. DEVELOPMENT OF THE GSW ALGORITHM

Becker and Li [8] proposed a split-window algorithm, and then Wan and Dozier [9] extended this algorithm to estimate LST from MODIS measurements with Viewing Zenith Angle (VZA) up to 69°. The extended algorithm is so called the GSW algorithm, and it is given by

$$\mathrm{LST} = C + (A_1 + A_2\frac{1-\varepsilon}{\varepsilon} + A_3\frac{\Delta\varepsilon}{\varepsilon^2})\frac{T_i+T_j}{2} + (B_1 + B_2\frac{1-\varepsilon}{\varepsilon} + B_3\frac{\Delta\varepsilon}{\varepsilon^2})\frac{T_i-T_j}{2} \quad (1)$$

with $\varepsilon = (\varepsilon_i + \varepsilon_j)/2$ and $\Delta\varepsilon = \varepsilon_i - \varepsilon_j$. where T_i and T_j are, the brightness temperatures (BTs) in Kelvin at top-of-atmosphere (TOA) in bands i (centered at around 11.0 μm) and j (centered at around 12.0 μm), respectively. ε_i and ε_j are, respectively, the Land Surface Emissivities (LSEs) in bands i and j, and C, A_1, A_2, A_3, B_1, B_2, B_3 are algorithm coefficients. For Landsat-8, i and j correspond to the TIRS bands 10 and 11, respectively.

In order to obtain the seven coefficients in Equation (1), it requires a large number of collocated, coincident and co-angled measurements of LST, LSEs and BTs in the TIRS bands 10 and 11. In reality, it is difficult to obtain a sufficient number of representative in-situ measurements on a global scale. A feasible and effective solution is to use the radiative transfer modeling experiment, which is conducted by the moderate spectral resolution atmospheric transmittance

TABLE 3. The regression results of equation (1) with the simulated data set for TPW sub-ranges.

TPW (cm)	C	A_1	A_2	A_3	B_1	B_2	B_3	R^2	RMSE (K)
[0.0, 2.0]	-0.925 ±0.060	1.00141 ±0.00024	0.17973 ±0.00142	-0.32651 ±0.00206	4.101 ±0.057	-4.380 ±1.623	23.693 ±1.263	0.9999	0.24
[1.5, 3.5]	6.575 ±0.479	0.97598 ±0.00174	0.11949 ±0.00484	-0.28565 ±0.00531	3.954 ±0.083	22.074 ±2.209	22.135 ±2.372	0.9983	0.43
[3.0, 5.0]	26.467 ±1.250	0.90635 ±0.00443	0.06771 ±0.01002	-0.07087 ±0.01381	4.864 ±0.120	14.212 ±2.684	-10.960 ±3.847	0.9953	0.60
[4.5, 7.8]	44.396 ±2.004	0.83976 ±0.00712	0.06830 ±0.01766	0.00286 ±0.02501	6.052 ±0.174	4.273 ±3.778	-16.171 ±5.566	0.9935	0.64

algorithm and computer model (MODTRAN) [21] fed with currently available atmospheric data set, and possible combinations of LST, LSEs and VZA [9], [11]. In this work, the SeeBor V5.0 database (http://cimss.ssec.wisc.edu) serves as the input atmospheric profiles in the radiative transfer modeling experiment. The SeeBor V5.0 training database, established by University of Wisconsin, consists of 15704 global profiles of temperature, moisture, and ozone at 101 pressure levels for clear sky condition (the relative humidity is less than 99%). The profiles are taken from NOAA-88, an European Centre for Medium-range Weather Forecasts (ECMWF) 60L training set, TIGR-3, ozonesondes from 8 NOAA Climate Monitoring and Diagnostics Laboratory (CMDL) sites, and radiosondes from 2004 in Sahara Desert. Over land surfaces, there are 8429 profiles, and the temperature of atmosphere adjacent to land surface, namely the boundary temperature (T_0), ranges between 200.2 and 318.5 K, while the Total Precipitable Water (TPW) varies from 0.1 to 7.8 cm.

The TIRS instrument observes the Earth surfaces in push-broom mode. Its swath width is about 185 km, and the maximum VZA is about 7.5°. Radiative transfer simulation shows that the BT difference in TIRS bands between 0° and 7.5° is about 0.02 K on average, which can be ignored. Therefore, only a nadir VZA is considered in the radiative transfer modeling experiment. With qualified atmospheric profiles extracted from the SeeBor V5.0 database, combined with spectral range and VZA, MODTRAN calculates the spectral transmittance, spectral upwelling radiance and spectral downwelling radiance, and then the MODTRAN's outputs are convolved with the SRFs of the TIRS bands 10 and 11 to obtain the band-averaged atmospheric quantities.

For given LST, LSEs and band-averaged atmospheric quantities, the BTs in the TIRS bands 10 and 11 at TOA can be simulated using the radiative transfer equation (RTE) [11]. The LST and LSEs are set as follows: for each atmospheric profile, LST goes from T_0-5 to T_0+20 K with a step of 5 K, and the mean of LSEs (ε) changes from 0.90 to 1.0 with a step of 0.02, while the LSE difference varies from -0.025 to 0.015 with a step of 0.005. Noted that, to convert between radiance in mW/m^2-sr-cm^{-1} and BT in Kelvin, look-up tables with a BT step of 0.1 K are established using Plank equation and the SRFs of TIRS bands 10 and 11. When the simulated data set of LST related to TPW, BTs and LSEs in TIRS bands is established, the seven coefficients in Equation (1) can be determined with multi-variable linear regression [22].

To improve the fitting accuracy of multi-variable linear regression, in terms of the number of simulated samples, TPW is empirically grouped into four sub-ranges with an overlap of 0.5 cm: [0, 2.0], [1.5, 3.5], [3.0, 5.0] and [4.5, 7.8] cm. For each TPW sub-range, a set of coefficients in Equation (1) are obtained, and the regression results are listed in Table 3. The regression Root Mean Square Error (RMSE), ranging between 0.24 and 0.64 K, is proportional to TPW, while the opposite is observed for the determinant coefficient (R^2), which decreases from 0.9999 to 0.9935.

To further improve the fitting accuracy of multi-variable linear regression, besides the groups of TPW, LST (T_s) also is empirically divided into four sub-ranges with an overlap of 5.0 K: $\leq$ 282.5, [277.5, 297.5], [292.5, 312.5], $\geq$ 307.5 K. For each TPW and LST sub-range, a set of coefficients also are obtained, and the regression results are given in Table 4. The RMSE, varying from 0.19 to 0.74 K, increases with both LST and TPW. In general, the RMSEs for LST and TPW sub-ranges are lower than that for TPW sub-ranges, and the accuracy of the GSW algorithm is better than 0.8 K.

When the GSW algorithm has been developed, LST will be derived in two steps: First, approximate LST is estimated using the coefficients of TPW sub-ranges according to input TPW. Then, more accurate LST is retrieved with the coefficients of LST and TPW sub-ranges according to input TPW and the approximate LST retrieved in the first step.

B. THE ESTIMATION OF LAND SURFACE EMISSIVITIES

In Equation (1), the LSEs in the TIRS bands 10 and 11 are two key input parameters to retrieve LST. LSEs, unlike sea surface emissivity, can differ significantly from unity and vary with vegetation, surface moisture, roughness, and viewing angle [23]. To date, various methods have been proposed to derive LSE from space. Several use the statistical relationships between the measurements and the LSEs, e.g., the classification-based emissivity method [24], and the Normalized Difference Vegetation Index (NDVI) based emissivity method (NBEM) [25]–[28]; others use reasonable assumptions or constraints in terms of Planck's function and the atmospheric RTE to solve the undetermined problem or the ill-posed inversion process, e.g., the day/night temperature independent spectral indices method [29], the physics-based

TABLE 4. The regression results of equation (1) with the simulated data set for LST and TPW sub-ranges.

LST (K)	TPW (cm)	C	A_1	A_2	A_3	B_1	B_2	B_3	R^2	RMSE (K)
≤282.5	[0.0, 2.0]	-3.674 ±0.060	1.01327 ±0.00024	0.17219 ±0.00134	-0.29474 ±0.00392	3.443 ±0.080	8.062 ±2.198	10.885 ±2.183	0.9999	0.19
	[1.5, 3.5]	48.342 ±2.267	0.82145 ±0.00816	0.11922 ±0.01111	-0.22574 ±0.01793	4.082 ±0.428	5.936 ±13.998	-39.435 ±16.338	0.9858	0.38
[277.5, 297.5]	[0.0, 2.0]	2.145 ±0.374	0.99179 ±0.00134	0.17066 ±0.00302	-0.27542 ±0.00427	3.884 ±0.101	-2.216 ±2.868	38.338 ±2.138	0.9980	0.24
	[1.5, 3.5]	2.441 ±0.754	0.99056 ±0.00271	0.11868 ±0.00582	-0.24989 ±0.00618	4.134 ±0.148	17.567 ±4.350	37.166 ±4.747	0.9936	0.40
	[3.0, 5.0]	29.179 ±2.452	0.89559 ±0.00864	0.11323 ±0.01701	-0.10097 ±0.02163	5.587 ±0.327	-12.098 ±8.581	23.233 ±11.453	0.9731	0.58
[292.5, 312.5]	[0.0, 2.0]	-1.757 ±0.517	1.00443 ±0.00179	0.18767 ±0.00453	-0.29613 ±0.00492	4.253 ±0.103	-11.781 ±2.815	40.982 ±2.160	0.9983	0.23
	[1.5, 3.5]	8.974 ±0.895	0.96741 ±0.00312	0.13675 ±0.00787	-0.30350 ±0.00767	4.229 ±0.124	14.274 ±3.286	41.933 ±3.532	0.9946	0.39
	[3.0, 5.0]	21.029 ±1.637	0.92480 ±0.00571	0.07703 ±0.01404	-0.08576 ±0.01953	4.914 ±0.180	11.027 ±4.238	-3.489 ±6.044	0.9883	0.55
	[4.5, 7.8]	43.700 ±2.228	0.84216 ±0.00788	0.07702 ±0.02163	-0.01111 ±0.03051	6.086 ±0.229	1.309 ±5.109	-11.109 ±7.317	0.9867	0.57
≥307.5	[0.0, 2.0]	1.940 ±0.782	0.99188 ±0.00259	0.19499 ±0.00774	-0.30794 ±0.0109	4.041 ±0.193	-7.203 ±5.166	36.127 ±4.022	0.9986	0.22
	[1.5, 3.5]	9.519 ±1.453	0.96150 ±0.00485	0.16270 ±0.02146	-0.46222 ±0.01797	5.188 ±0.214	7.461 ±5.27698	63.072 ±4.479	0.9956	0.38
	[3.0, 5.0]	47.104 ±3.138	0.83239 ±0.01082	0.16008 ±0.04288	-0.22070 ±0.05686	5.826 ±0.334	-1.34731 ±6.81881	11.203 ±9.919	0.9888	0.62
	[4.5, 7.8]	69.398 ±5.200	0.75109 ±0.01869	0.22952 ±0.10293	-0.08277 ±0.11141	6.854 ±0.618	-14.99269 ±13.5359	-6.143 ±16.770	0.9826	0.74

day/night method [30], and the temperature emissivity separation method [31]. Taking full consideration of the advantages and disadvantages of existing LSE estimation methods and the technical specifications of TIRS and OLI on Landsat-8, the modified NBEM method [27] is adopted in this work, and for Landsat-8 data, it is

$$\varepsilon_i = \begin{cases} a_{1i} + \sum_{j=2}^{7} a_{ji}\rho_j & \text{NDVI} < \text{NDVI}_\text{s} \\ \varepsilon_{\text{v},i}P_\text{v} + \varepsilon_{\text{s},i}(1-P_\text{v}) + C_i & \text{NDVI}_\text{s} \le \text{NDVI} \le \text{NDVI}_\text{v} \\ \varepsilon_{\text{v},i} + C_i & \text{NDVI} > \text{NDVI}_\text{v} \end{cases} \quad (2)$$

where ε_i is the estimated LSE in the TIRS band i ($i = 10$ or 11), $\varepsilon_{\text{v},\,i}$ and $\varepsilon_{\text{s},\,i}$ denote LSEs of vegetation and bare soil, respectively, ρ_j is the apparent reflectance in the OLI band j, $a_{1i} \sim a_{7i}$ are unknown coefficients, and P_v is the fractional vegetation cover, which is given by [32]

$$P_\text{v} = \left[\frac{\text{NDVI} - \text{NDVI}_\text{s}}{\text{NDVI}_\text{v} - \text{NDVI}_\text{s}}\right]^2 \quad (3)$$

where NDVI_s and NDVI_v, respectively, stand for the NDVI of bare soil and vegetation, and typically, $\text{NDVI}_\text{s} = 0.2$ and $\text{NDVI}_\text{v} = 0.5$ for global conditions [26]. It is set to zero for measurements with $\text{NDVI} \le \text{NDVI}_\text{s}$, and set to one for measurements with $\text{NDVI} \ge \text{NDVI}_\text{v}$.

The term C_i is the cavity effect of mixed natural surfaces due to surface roughness ($C_i = 0$ for flat surface), and it is [33]

$$C_i = (1 - \varepsilon_{s,i})\varepsilon_{\text{v},i}F'(1 - P_\text{v}) \quad (4)$$

where F' is a geometrical factor ranging between zero and one, depending on the geometrical distribution of land surfaces, and a typical value of 0.55 is used [28]. When the NDVI is larger than NDVI_v, C_i is zero. To complement the cavity effect of homogeneous vegetation, a fixed value of 0.005 is recommended for C_i [26], [28].

To determine the unknown coefficients in Equation (2), first, spectral data of vegetation and bare soils are extracted from the Advanced Spaceborne Thermal Emission and Reflection Radiometer (ASTER) spectral library (http://speclib.jpl.nasa.gov) [34], and then they are convolved with the SRFs to obtain the reflectances in the OLI bands 2∼7 and LSEs in the TIRS bands 10 and 11. Because the LSE differences within the same type of materials are small, the mean values are calculated to substitute for $\varepsilon_{\text{v},i}$ and $\varepsilon_{\text{s},i}$ in Equation (2), i.e., $\varepsilon_{\text{v},10} = 0.982$, $\varepsilon_{\text{v},11} = 0.984$, $\varepsilon_{\text{s},10} = 0.971$, and $\varepsilon_{\text{s},11} = 0.976$. Finally, the coefficients $a_{1i} \sim a_{7i}$ in Equation (2) are determined by multi-variable linear regression. The regression results are listed in Table 5. For the TIRS bands 10 and 11, the correlation coefficients (R) are, respectively, 0.788 and 0.812, while RMSEs are, respectively, 0.003 and 0.002. Figure 2 shows the LSEs estimated by the modified NBEM method versus that extracted from the ASTER spectral library in the TIRS bands 10 and 11, and

TABLE 5. Results of multi-variable linear regression for the unknown coefficients in equation (3).

Band	a_1	a_2	a_3	a_4	a_5	a_6	a_7	R	RMSE
10	0.980±0.006	-0.140±0.065	0.170±0.112	-0.036±0.096	-0.083±0.078	0.158±0.044	-0.149±0.039	0.788	0.003
11	0.979±0.004	0.026±0.043	-0.071±0.075	0.048±0.064	-0.056±0.052	0.128±0.029	-0.105±0.026	0.812	0.002

TABLE 6. LST errors caused by NEΔT in TIRS bands 10 and 11.

LST (K)	TPW (K)	RMSE without NEΔT (K)	RMSE with NEΔT (K)	Increasing percentage (%)
⩽282.5	[0.0, 2.0]	0.19	0.29	52.6
	[1.5, 3.5]	0.38	0.51	34.2
[277.5, 297.5]	[0.0, 2.0]	0.24	0.33	37.5
	[1.5, 3.5]	0.40	0.51	27.5
	[3.0, 5.0]	0.58	0.69	19.0
[292.5, 312.5]	[0.0, 2.0]	0.23	0.34	47.8
	[1.5, 3.5]	0.39	0.51	30.8
	[3.0, 5.0]	0.55	0.70	27.3
	[4.5, 7.8]	0.57	0.76	33.3
⩾307.5	[0.0, 2.0]	0.22	0.30	36.4
	[1.5, 3.5]	0.38	0.48	26.3
	[3.0, 5.0]	0.62	0.78	25.8
	[4.5, 7.8]	0.74	0.92	24.3

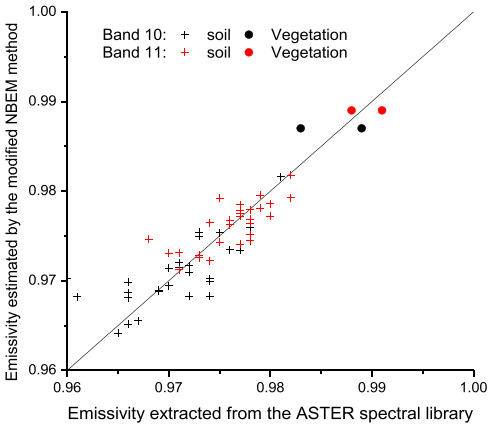

FIGURE 2. LSEs estimated by the NBEM method versus that extracted from ASTER Spectral Library in TIRS bands 10 and 11.

they are basically distributed around diagonals. The accuracy of LSEs estimated by the modified NBEM method satisfy the requirement of LST retrieval.

C. SENSITIVITY ANALYSIS

BTs, LSEs and TPW are major input parameters to the GSW algorithm, and their uncertainty will influence the derived LST.

The errors of TIRS measurements mainly come from radiometric calibration and the NEΔT. The biases of radiometric calibration in the TIRS bands 10 and 11 will be corrected in section III, so only NEΔT is discussed here. Supposing that the NEΔT obeys normal distribution, Gaussian noises with zero mean and standard deviation equal to two times of NEΔT are added to the simulated BTs. LST is again retrieved with the NEΔT-contaminated BTs, and the impact of NEΔT is evaluated. The RMSEs with and without NEΔT are listed in Table 6.

In contrast to RMSEs without NEΔT, the RMSEs with NEΔT increased by 0.09 to 0.19 K, or in percentage from 19.0% to 52.6%. The absolute increment of RMSE with NEΔT is proportional to LST and TPW, whereas the increasing percentage is not. Generally, the influence of NEΔT on LST retrieval is weak.

LSEs play an important role in LST retrieval. As reported in [35], the uncertainty of LSEs derived from satellite measurements is about 1%. To assess its impact on LST, 1% uncertainty is introduced into LSEs in the TIRS bands 10 and 11, and then LST is derived with the LSEs with 1% uncertainty. The results in Table 7 indicate that the RMSE with LSEs uncertainty increased by 0.08 to 0.53 K. The RMSE increment is inversely proportional to TPW, whereas it increases with LST, i.e., the impact of LSE uncertainty on LST is much stronger for dry and hot atmosphere.

As for TPW, assuming that the TPW uncertainty is ±0.5 cm, TPW on the border of sub-ranges might be incorrectly grouped into its neighboring sub-range, which will lead to inaccurate LST retrieval. The RMSEs before and after incorrect TPW grouping are listed in Table 8. The increment of RMSEs varies from 0.02 to 0.33 K. The impact of TPW uncertainty on LST retrieval is stronger than NEΔT does, whereas it is weaker than the influence of LSEs uncertainty.

D. COMPARISON WITH OTHER SPLIT-WINDOW ALGORITHMS

At present, there are other three kinds of split-window algorithms developed to retrieve LST from Landsat-8 data. The first one was proposed by Jiménez-Muñoz *et al.* [18] based

TABLE 7. LST errors caused by 1% uncertainty in land surface emissivities.

LST (K)	TPW (cm)	RMSE without LSE uncertainty (K)	RMSE with 1% uncertainty in LSEs (K)	Increment of RMSE (K)
≤282.5	[0.0, 2.0]	0.19	0.51	0.32
	[1.5, 3.5]	0.38	0.58	0.20
[277.5, 297.5]	[0.0, 2.0]	0.24	0.59	0.35
	[1.5, 3.5]	0.40	0.59	0.19
	[3.0, 5.0]	0.58	0.68	0.10
[292.5, 312.5]	[0.0, 2.0]	0.23	0.67	0.44
	[1.5, 3.5]	0.39	0.70	0.31
	[3.0, 5.0]	0.55	0.70	0.15
	[4.5, 7.8]	0.57	0.65	0.08
≥307.5	[0.0, 2.0]	0.22	0.75	0.53
	[1.5, 3.5]	0.38	0.81	0.43
	[3.0, 5.0]	0.62	0.88	0.26
	[4.5, 7.8]	0.74	0.97	0.23

TABLE 8. Root mean square errors in LST retrieval caused by TPW uncertainty.

TPW (cm)	[0.0, 2.0]	[1.5, 3.5]	[3.0, 5.0]	[4.5, 7.8]
[0.0, 2.0]	0.23	0.45		
[1.5, 3.5]	0.39	0.37	0.70	
[3.0, 5.0]		0.77	0.52	0.60
[4.5, 7.8]			0.77	0.47

TABLE 9. Comparison of root mean square errors of different split-window algorithms for TPW sub-ranges (Unit: Kelvin).

TPW (cm)	Jiménez-Muñoz	Rozenstein	GSW with quadratic term	GSW in this work
[0.0, 2.0]	0.34	0.31	0.24	0.24
[1.5, 3.5]	0.33	0.55	0.42	0.43
[3.0, 5.0]	0.47	1.17	0.59	0.60
[4.5, 7.8]	0.60	2.06	0.63	0.64

on the structure suggested by Sobrino *et al*. [36], and it is given by

$$T_s = T_i + d_1(T_i - T_j) + d_2(T_i - T_j)^2 + d_0 + (d_3 + d_4 w)(1 - \varepsilon) + (d_5 + d_6 w)\Delta\varepsilon \quad (5)$$

where d_k ($k = 0, 1, \ldots, 6$) is the algorithm coefficient, and w is the TPW.

The second split-window algorithm was developed by Rozenstein *et al*. [17], and it can be written as follows:

$$T_s = T_i + f_0(T_i - T_j) + e_1 f_1 + e_2 f_2 + e_3 f_1 T_i - e_4 f_2 T_j \quad (6)$$

where e_k ($k = 1, 2, 3$ or 4) is algorithm coefficient, and f_0 and f_1 are functions of atmospheric transmittance and LSEs in bands i and j.

The third one is a new refinement of the GSW algorithm, in which a quadratic term of $(T_i - T_j)$ is added [37]. To compare the above three split-window algorithms with the GSW algorithm in this work, the simulated data set in section II is used to determine the algorithm coefficients for each TPW and LST sub-range, and meanwhile the RMSEs are calculated. The comparison of RMSEs of different split-window algorithms for all TPW and LST sub-ranges are listed in Tables 9 and 10. For convenience, the RMSEs of the GSW algorithm in this work are also list in the tables. The RMSEs are generally proportional to TPW and LST. The GSW algorithm in this work is consistent with Jiménez-Muñoz's algorithm, with RMSE varying from 0.2 to 0.7 K, whereas it is much more accurate than Rozenstein's algorithm, whose RMSE is up to 2.1 K. Further investigation reveals that the split-window algorithm proposed by Rozenstein *et al* [17] produces large errors for extremely humid atmosphere, which leads to low accuracy on average. The results also indicate that the GSW algorithms with and without quadratic term have no obvious difference.

TABLE 10. Comparison of root mean square errors of different split-window algorithms for LST and TPW sub-ranges (Unit: Kelvin).

LST (K)	TPW (cm)	Jiménez-Muñoz	Rozenstein	GSW with quadratic term	GSW in this work
≤282.5	[0.0, 2.0]	0.27	0.31	0.19	0.19
	[1.5, 3.5]	0.20	0.32	0.38	0.38
[277.5, 297.5]	[0.0, 2.0]	0.20	0.28	0.24	0.24
	[1.5, 3.5]	0.25	0.43	0.40	0.40
	[3.0, 5.0]	0.34	0.93	0.58	0.58
[292.5, 312.5]	[0.0, 2.0]	0.22	0.28	0.22	0.23
	[1.5, 3.5]	0.30	0.55	0.38	0.39
	[3.0, 5.0]	0.39	1.12	0.54	0.55
	[4.5, 7.8]	0.49	2.04	0.55	0.57
≥307.5	[0.0, 2.0]	0.25	0.25	0.21	0.22
	[1.5, 3.5]	0.33	0.60	0.36	0.38
	[3.0, 5.0]	0.59	1.26	0.59	0.62
	[4.5, 7.8]	0.72	2.18	0.73	0.74

III. DATA DESCRIPTION AND PROCESSING

A. LANDSAT-8 L1 DATA

In this work, the main data are the geo-located and calibrated Landsat-8 L1 product, which is downloaded from the website of United States Geological Survey (USGS) (http://landsat.usgs.gov). The Landsat-8 L1 product, in World

Reference System 2 (WRS-2) and GeoTIFF file format, provides visible and near infrared measurements in the OLI bands 1∼9 and thermal infrared measurements in the TIRS bands 10 and 11, Quality Assessment (QA), and meta data. The thermal infrared measurements in the TIRS bands 10 and 11 are up-sampled from 100 meters to 30 meters to match OLI's measurements in space. For the OLI bands 1∼9, the following equation is applied to converting digital number into reflectance,

$$\rho_\lambda = M_\rho \times Q_{\text{cal}} + A_\rho \tag{7}$$

where ρ_λ is the reflectance at TOA, Q_{cal} is the Digital Number (DN), and M_ρ and A_ρ are, respectively, the multiplying and adding factors, which can be extracted from the meta data. Then the reflectance is corrected with solar elevation angle θ_s by

$$\rho'_\lambda = \rho_\lambda / \sin(\theta_s) \tag{8}$$

For the TIRS bands 10 and 11, a similar calibration equation is used

$$L_\lambda = M_L \times Q_{\text{cal}} + A_L \tag{9}$$

where L_λ is the radiance at TOA in W/m^2-sr-μm, and M_L and A_L are, respectively, the multiplying and adding factors, which can also be extracted from the meta data. The NDVI is calculated from the reflectances in OLI bands 4 and 5, and then LSEs in TIRS bands 10 and 11 are estimated using Equation (3). Water bodies are discriminated according to NDVI, whose value is usually less than zero. The cloudy measurements and those with ice/snow cover are removed in terms of the information extracted from the QA band.

B. INTER-CALIBRATION OF TIRS BANDS 10 AND 11

Former research reported that the measurements in the TIRS bands 10 and 11 are strongly affected by the out-of-field energy (stray light), especially for band 11 [38]. Therefore, the TIRS measurements should be re-calibrated before LST retrieval. As we know, the Infrared Atmospheric Sounding Interferometer (IASI) is a key payload element on the Metop series of European meteorological polar-orbiting satellites. It was developed by the Centre National d'Études Spatiales (CNES) in the framework of a cooperation agreement with the European Organisation for the Exploitation of Meteorological Satellites (EUMETSAT). The first flight model was launched in 2006 on board the first European operational meteorological polar-orbiting satellites, namely Metop-A. The second one mounted on the Metop-B satellite was launched in September 2012. The IASI instrument has 8,461 channels continuously covering the spectrum from the edge of the thermal infrared at 3.62 μ m (2760 cm^{-1}) up to 15.5 μ m (645 cm^{-1}) with a fixed unapodized spectral resolution of 0.25 cm^{-1}, and the spatial resolution at nadir is about 12 km. The IASI's in-orbit calibration has proven to be stable and consistent with that of Atmospheric Infrared Sounder (AIRS) on board Aqua, whose standard uncertainties is about 0.1 K ($k = 1$) [39]. Therefore, the TIRS bands 10 and 11 are inter-calibrated against IASI/Metop-B hyperspectral channels using the hyperspectral convolution (HSC) method [40]–[44]. An Arctic area (60°N–90° N, 180°W–180°E) shown in Figure 3 is selected as an inter-calibration area to obtain a sufficient number of collocated, coincident and co-angled measurements. Besides the Arctic Ocean, this inter-calibration area also contains Greenland and part of Asia, North America and Europe. According to the Global Land Cover 2000 (GLC2000) product generated by Institute for Environment and Sustainability (IES, http://bioval.jrc.ec.europa.eu/products/glc2000/products.php), this area is dominated by water bodies, ice and snow, which is beneficial to inter-calibration.

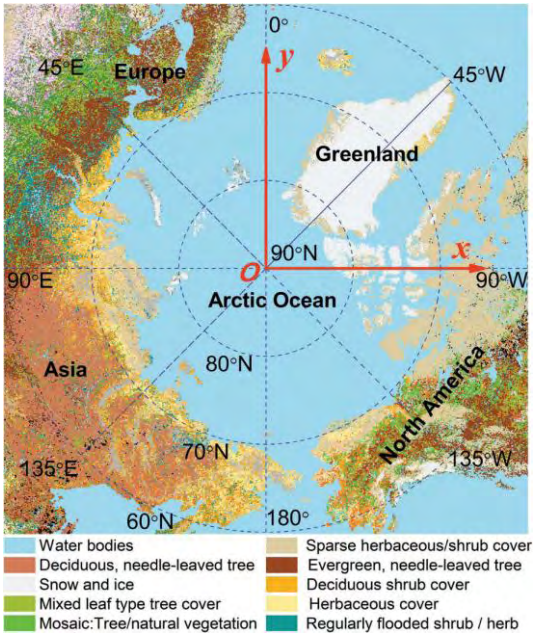

FIGURE 3. Inter-calibration study area (generated from GLC2000 product).

The Landsat-8 L1 data and IASI/Metop-B 1C data covering the inter-calibration area in July and August of 2015 are used. The IASI/Metop-B 1C data are provided by the NOAA Comprehensive Large Array-Data Stewardship System (CLASS, http://www.class.ngdc.noaa.gov). To match the TIRS and IASI measurements in space, first, an x-y Cartesian coordinate system is set up (Figure 3), and longitude (α) and latitude (β) in degree are converted into x-y as follows:

$$\begin{cases} x = (90^\circ - |\beta|)\cos\zeta \\ y = (90^\circ - |\beta|)\sin\zeta \end{cases} \tag{10}$$

with $\zeta = 90^\circ - \vartheta$ for $\vartheta \le 90^\circ$ or $\zeta = 450^\circ - \vartheta$ otherwise, and $\vartheta = \alpha$ for $\alpha \ge 0^\circ$ or $\vartheta = \alpha + 360^\circ$ otherwise.

Then, the inter-calibration area is gridded with Δx and Δy equal to 0.2. Finally, all the data, including TIRS and IASI's radiances, VZA and observation time, are pixel-aggregated into the discretized area using area-weighting interpolation method.

After pixel-aggregation, the gridded TIRS and IASI measurements are put into the same x-y discrete coordinate

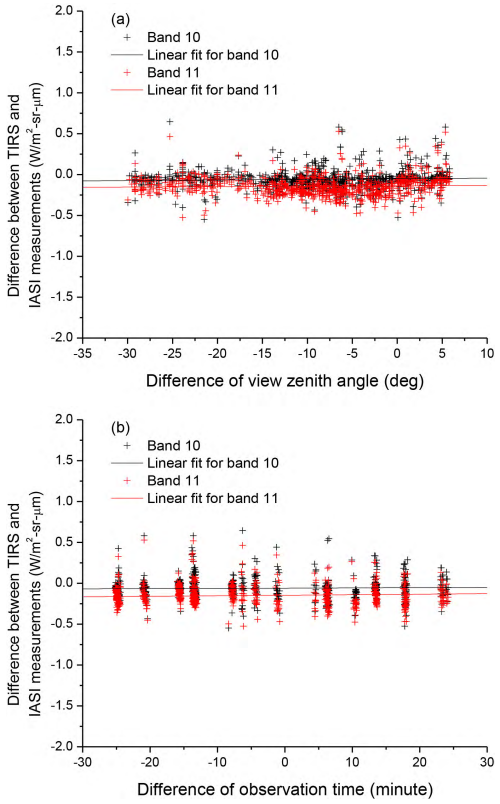

FIGURE 4. Measurement differences in bands 10 and 11 versus viewing zenith angle difference (a). and observation time difference (b).

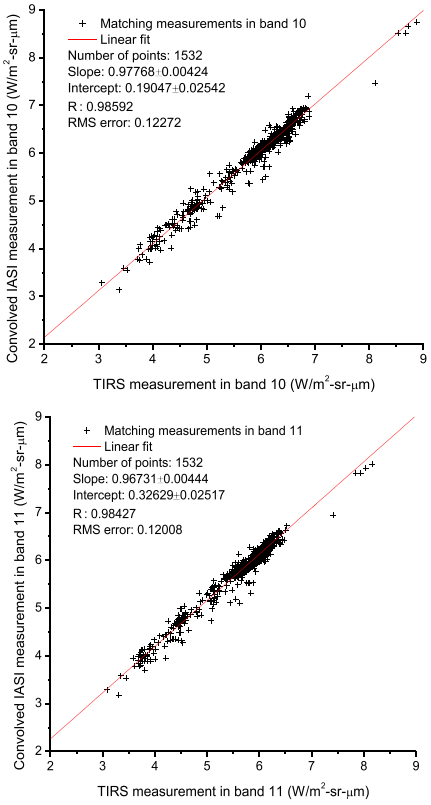

FIGURE 5. TIRS-IASI matching measurements in the TIRS bands 10 and 11 and linear fit results.

system, i.e., the measurements over the same pixel-aggregated grid are collocated. The coincident and co-angled criteria are satisfied with difficulty for actual TIRS and IASI measurements, and they are usually replaced by approximations: the absolute observation time difference ($|\Delta\text{time}|$) and absolute VZA difference ($|\Delta\text{VZA}|$) are less than given thresholds [42]–[44]. Figure 4 displays the radiance differences between matching TIRS and IASI measurements varying with VZA difference (ΔVZA) and observation time difference (Δtime). The radiance difference mainly ranges between ± 0.5 W/m^2-sr-μm (approximately ± 6.0 K), and they have no obvious increase or decrease trend when ΔVZA goes from -30° to 8° and Δtime varies from -25 to 25 minutes. Moreover, the linear fit lines are almost horizontal, which indicates that the dependence of radiance differences on ΔVZA and Δtime is weak. Based on the results in Figure 4, the following matching criteria are applied: the collocation over the pixel-aggregated grid, $|\Delta\text{time}| < 25$ minutes, and $|\Delta\text{VZA}| < 30°$. Furthermore, to mitigate the influence of surface inhomogeneity, an extra criterion is used: the maximum absolute BT difference in the 3×3 neighborhood centered at the matching measurement in an image is less than 5.0 K.

With the matching criteria given above, a total of 1532 TIRS-IASI matching measurements are collected. Taking the TIRS measurements as x and IASI measurements as y, the matching measurements, ranging between 3.0 and 9.0 W/m^2-sr-μm, are displayed in Figure 5. The TIRS measurement is highly linearly related to the convolved IASI measurement: the correlation coefficients (R) are greater than 0.984, and RMSEs are 0.12272 and 0.12008 W/m^2-sr-μm for the TIRS bands 10 and 11, respectively. In general, the calibrations of both TIRS bands 10 and 11 are biased against the IASI hyperspectral channels, however TIRS band 10 agrees with IASI hyperspectral channels relatively much better. Inter-calibration coefficients (slope and intercept) for TIRS bands 10 and 11 are obtained through linear fits on the matching measurements (Figure 5).

In terms of the inter-calibration coefficients given in Figure 5, all the TIRS measurements are re-calibrated. To demonstrate the inter-calibration effects, Figure 6 shows the histograms of BT differences between TIRS and IASI matching measurements before and after re-calibration. The BT differences, mainly ranging between ± 6.0 K, basically obey normal distribution. Before re-calibration, in contrast to histogram in the TIRS band 10, the histogram center for band 11 more obviously deviates from zero, and its distribution is much disperser. On average, the calibration biases in the TIRS bands 10 and 11 are, respectively, -0.54 ± 1.21 K and -1.52 ± 1.35 K against the IASI measurements. After re-calibration, both histograms in the TIRS bands 10 and 11 are centered at zero. The results in Figure 6 indicate that the

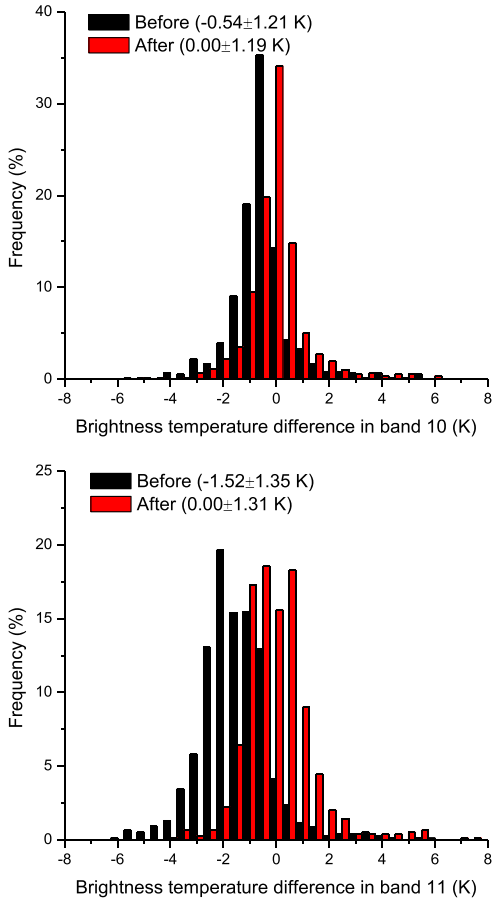

FIGURE 6. Histograms of brightness temperature differences between the TIRS-IASI matching measurements in TIRS bands 10 and 11 before and after re-calibration (the bin size is 0.5 K).

calibration of IASI hyperspectral channels has been successfully transferred to the TIRS bands 10 and 11.

IV. APPLICATION OF LST RETRIEVAL FROM LANDSAT-8 DATA

The GSW algorithm is applied to LST retrieval from Landsat-8 data in 2015. BTs and LSEs in the TIRS bands 10 and 11, TPW and cloud mask are four input parameters to retrieve LST. BTs in the TIRS band 10 and 11 and cloud mask are extracted from Landsat-8 L1 data, and then the TIRS measurements are re-calibrated using the inter-calibration coefficients in Figure 5. LSEs in the TIRS bands 10 and 11 are estimated from the OLI data by the modified NBEM method developed in Section II. TPW is extracted from temporally and spatially nearest $0.025° \times 0.025°$ ECMWF reanalysis data, and then they are spatially resampled into the Landsat-8 swath using bilinear interpolation method.

With the input of BTs and LSEs in the TIRS bands 10 and 11, TPW and cloud mask, LSTs in 2015 are retrieved using the developed GSW algorithm in this work. Taking the Landsat-8 swath acquired at 2:27 UTC on July 19 of 2015 over a Northeast China area centered at

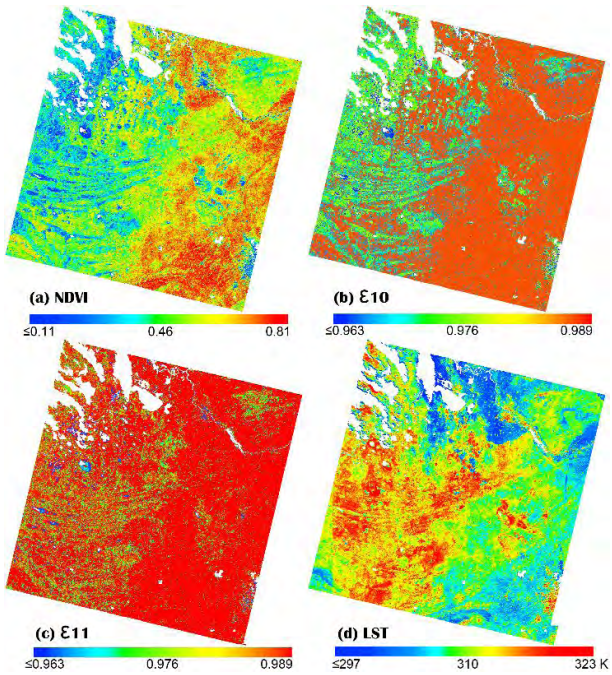

FIGURE 7. Maps of NDVI (a), LSEs in TIRS bands 10 and 11 (b and c) and LST (d) derived from Landsat-8 data acquired at 2:27 UTC on July 19 of 2015 over a Northeast China area centered at (44.594°N, 124.336°E) (swath path = 119 and row = 29 in WRS-2).

(44.594°N, 124.336°E) (swath path = 119 and row = 29 in WRS-2) as example, Figure 7 demonstrates the NDVI, LSEs in bands 10 (ε_{10}) and 11 (ε_{11}) and LST derived from Landsat-8 L1 data. The NDVI changes from 0.11 to 0.81, and LSEs range between 0.963 and 0.989, while LSTs are distributed between 297 and 323 K. The NDVI over densely vegetated areas are higher than that over sparsely vegetated and bare areas, and LSEs have positive correlation with NDVI. The LST over bare areas (low NDVI) is usually higher than that over vegetated areas (relatively higher NDVI) due to the relative low thermal inertia of bare areas.

V. CROSS-VALIDATION AND ANALYSIS

In this work, the derived LST is cross-validated against the MODIS/Terra LST and Emissivity (LST/E) product MOD11_L2 V6. The MOD11_L2 V6 product is a 5-min level-2 swath 1 km data set and covers both daytime and nighttime observations. The MOD11_L2 V6 product is generated from clear sky MODIS/Terra L1B data using the GSW algorithm [9], whereas LSEs are estimated by classification-based emissivity method [24]. Besides LST and LSEs, the MOD11_L2 V6 product also provides longitude and latitude, observation time, VZA and quality assurance. The validation with in-situ measurements indicated that the MOD11_L2 product is better than 1.0 K for most cases [37], [45].

Cross-validation requires collocated and coincident LST. For two polar-orbit satellites, to obtain a sufficient number of collocated and coincident measurements, the study area

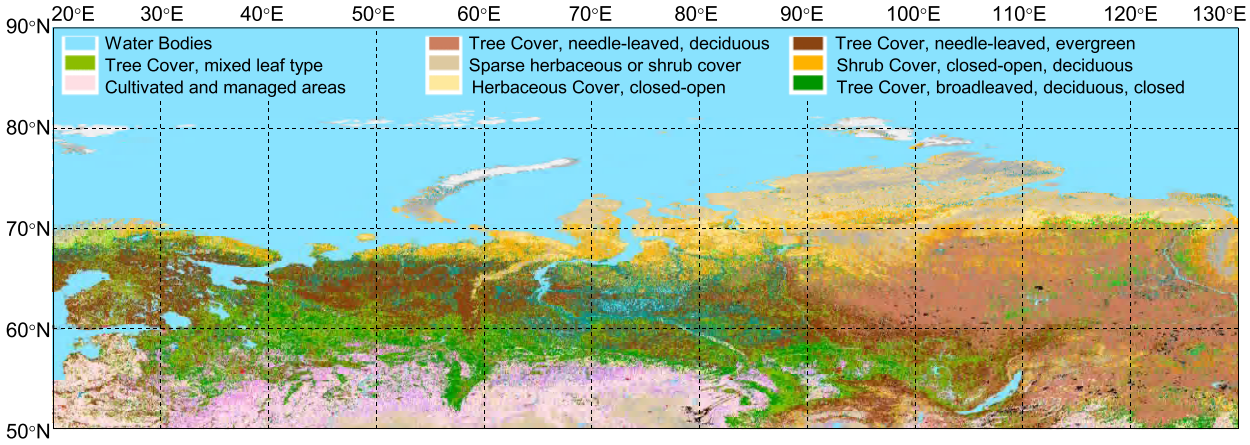

FIGURE 8. Eurasian area for LST cross-validation (generated from GLC2000).

should be located as high a latitude as possible [46]. The Arctic and Antarctic regions satisfy this condition, however most of the two areas are covered by ice and snow all the year round, and they are not good places for LST validation in this work. Taking full consideration of the matching criteria, land cover diversity and feasibility, an area of the Eurasian continent with latitude larger than 50°N and longitude from 20°E to 130°E is selected for cross-validation (Figure 8). According to the GLC2000 product, the main land cover types are tree cover, sparse herbaceous cover, shrub cover, and cultivated and managed area.

As we know, the sizes of pixels in Landsat-8 L1 data product are 30×30 meters in equal area Universal Transverse Mercator (UTM) projection, whereas the MOD11_L2 V6 product is a 5-min swath 1-km data set in longitude and latitude coordinate system. To match the LST in space, first, the data extracted from the MOD11_L2 V6 product are geometrically transformed into the equal area UTM projection system (the MOD11_L2 pixel in equal area UTM system is an irregular quadrilateral), and then the LST derived from Landsat-8 data, as well as the observation time and VZA, are resampled into the irregular MOD11_L2 pixel using area-weighting interpolation method.

Based on the trade-off between uncertainty and the number of matching LST, the following criteria are selected to collect matching LST: collocation over the irregular MOD11_L2 pixel in the equal area UTM projection, the absolute observation time difference of less than 35 min ($|\Delta\text{time}| < 35$'), and the absolute VZA difference of less than 35° ($|\Delta\text{VZA}| < 35°$).

Besides the above three major matching criteria, several factors are also necessarily taken into account. Although the MOD11_L2 LST and LST in this work are derived under the so-called ''clear sky'' conditions, the effects of unfiltered clouds cannot be ignored. If a pixel in a 3×3 window centered at the matching pixel is labeled as cloudy or possible cloudy, the matching LST will be discarded. To eliminate impact of water and ice/snow, if a pixel in 3×3 window centered at the matching pixel is along water or ice/snow boundary, the matching LST is also abandoned. Moreover, to mitigate the influence of heterogeneity of land surface properties, the maximum LST difference in a 3×3 window centered at the matching pixel within an image is required to be less than 2.0 K.

The collection of matching LST is carried out in three steps. First, the Landsat-8 swaths and MOD11_L2 are approximately matched according to covering area and acquisition time. Sixteen matching swaths of Landsat-8 and MOD11_L2 V6 from July 11 to September 22 in 2015 over the cross-validation area are qualified. Taking the Landsat-8 data at 6:00 UTC on August 6 of 2015 (swath row $=$ 6 and path $=$ 155 in WRS-2) and MOD11_L2 V6 product at 5:30 UTC on the same day as example, Figure 9 shows the comparison of LST derived from Landsat-8 data in this work and that extracted from MOD11_L2 V6 product over the same area (red boxed region in Figure 9(c)). Although the observation time difference is up to 30 minutes, and VZA also is different, the LST derived from Landsat-8 data (Figure 9(a)) is quite consistent with that extracted from MOD11_L2 V6 product (Figure 9(b)), not only for spatial distribution, but also for the values of LST. Then, the LST derived from Landsat-8 data is resampled over MOD11_L2 V6 pixels in equal area UTM projection system. Finally, in terms of the matching criteria, matching LST is collected from the matching swaths through pixel by pixel search.

With the above criteria, 18106 matching LSTs over the MOD11_L2 V6 pixels in equal area UTM projection system are collected. Figure 9(a) shows the LST derived from Landsat-8 data in this work versus that extracted from MOD11_L2 V6 product. The matching LST ranges between 280.0 and 301.0 K. The LST derived from Landsat-8 data is highly linearly related to that extracted from MOD11_L2 V6 product with a correlation coefficient R of 0.973. Against MOD11_L2 V6 product, the bias of LST in this work is -1.45 ± 0.80 K. Figure 10(b) displays the

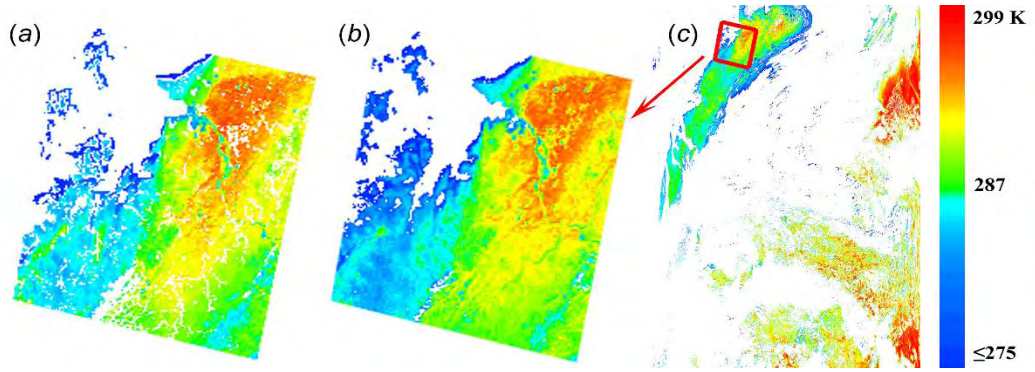

FIGURE 9. Comparison between the LST derived from Landsat-8 data in this work and that extracted from MOD11_L2 V6 product. (a) Map of LST derived from Landsat-8 data in this work resampled over MOD11_L2 V6 grid (6:00 UTC, August 6, 2015) (b) A close-up of red boxed region in (c) corresponding to the area in (a); (c) Map of LST extracted from MOD11_L2 V6 product (5:30 UTC, August 6, 2015).

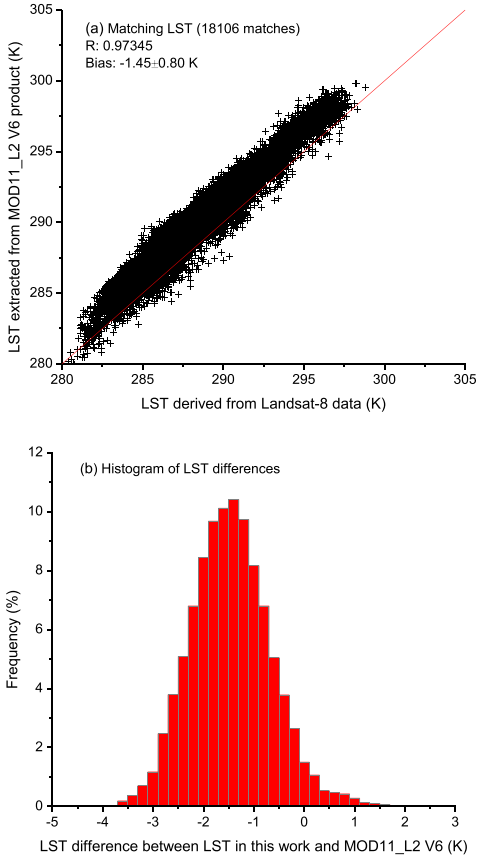

FIGURE 10. The LST derived from Landsat-8 data in this work versus that extracted from MOD11_L2 V6 product (a), and histogram of LST differences between LST retrieved in this work and that extracted MOD11_L2 V6 product (b).

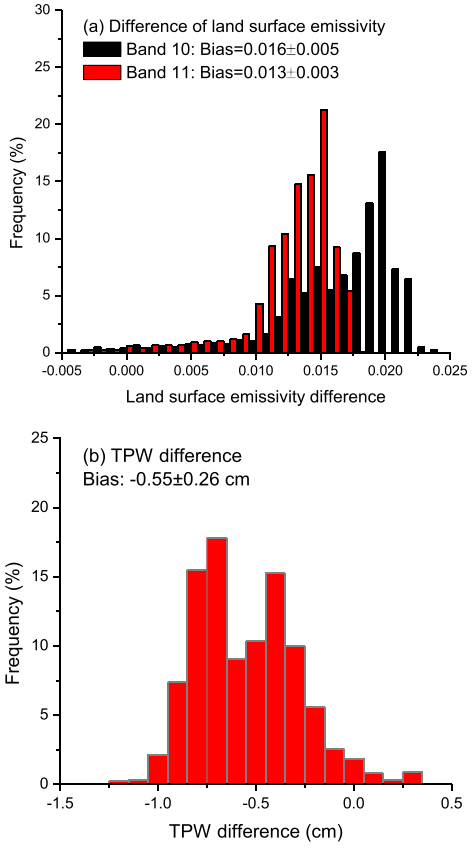

FIGURE 11. Histograms of land surface emissivity differences in TIRS bands 10 and 11 (a) between LSE in this work and that extracted from MOD11_L2 V6 product, and histogram of TPW difference between ECMWF reanalysis data and MOD07_L2 V6 product (b).

histogram of LST differences between LST in this work and that extracted from MOD11_L2 V6 product. The difference mainly varies from -4.0 to 1.5 K, and it basically obeys a normal distribution centered at about 1.4 K.

Recalling the sensitivity analysis in Section II, LST error mainly comes from the uncertainty of LSEs and TPW. To assess the actual impact of LSEs and TPW uncertainty on LST retrieval, we compute the differences between LSEs estimated from the OLI data by NBEM method in this work and that extracted from the MOD11_L2 V6 product, in which the spectral differences are removed by linear fits over typical samples extracted from the ASTER Spectral

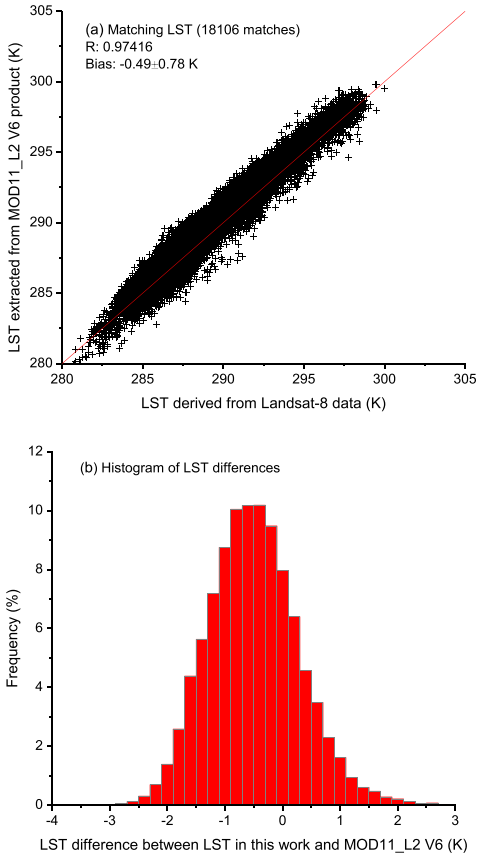

FIGURE 12. LST derived from Landsat-8 data versus that extracted from MOD11_L2 V6 product after LSEs and TPW correction (a), and histogram of LST differences between LST retrieved in this work and MOD11_L2 V6 LST (b).

Library, and we also calculate the TPW differences between the ECMWF reanalysis data and the MOD07_L2 V6 product. Figure 10 displays the histograms of LSE and TPW differences. The LSE difference ranges in [−0.005, 0.025] and [−0.005, 0.018] for the TIRS bands 10 and 11, respectively. In contrast to the MOD11_L2 V6 product, the LSEs in the TIRS bands 10 and 11 estimated by the NBEM method are averagely 0.016±0.005 and 0.013±0.003 overestimated, which leads to LST underestimate of 0.5∼1.0 K. The TPW differences changes from −1.25 to 0.4 cm, and in contrast to the MOD07_L2 V6 product, the TPW bias of ECMWF reanalysis data is −0.55±0.26 cm, which also leads to LST underestimate of about 0.5 K in this work.

If the LSEs in the TIRS bands 10 and 11 and TPW extracted from the ECMWF reanalysis data are, respectively, corrected with the biases calculated in Figure 11, in theory, the LST in this work will be much more consistent with that extracted from the MOD11_L2 V6 product. Figure 12(a) shows the LST in this work after LSEs and TPW correction versus LST extracted from the MOD11_L2 V6 product. After correction, the matching LST is symmetrically distributed around the diagonal with a correlation coefficient of 0.974. In contrast to the MOD11_L2 V6 product, the bias of LST in this work after correction is −0.49±0.78 K. The histogram of LST differences in Figure 12(b) also obeys normal distribution, and the center is much closer to zero. Compared to the results before LSEs and TPW correction (Figure 10), the LST bias after LSEs and TPW correction decreased by about 1.0 K, i.e., the LST derived from Landsat-8 data is much more consistent with that extracted from the MOD11_L2 V6 product after the correction of LSEs and TPW.

Several research also developed split-window algorithms to retrieve LST from Landsat-8 data, and then validated the results with independent simulated data, MODIS LST or in-situ LST. Jiménez-Muñoz *et al*. [18] and Du *et al*. [47] validated the derived LST against independent simulated data, and RMSEs for the split-window algorithm over the whole TPW range are around 1.0 K, with almost no bias. Nikam *et al*. [48] cross-validated the retrieved LST with MODIS LST, and the bias is approximate 2.4 K. Wang *et al*. [49] validated the LST retrieved from Landsat-8 TIRS measurements against in-situ LST in an extremely arid region, and the RMSEs range from 1.7 K to 4.7 K. Compared to the results of previous research, the LST derived from Landsat-8 data in this work is accurate enough.

VI. CONCLUSION AND DISSCUSSION

The paper presented the development of the GSW algorithm to retrieve LST from Landsat-8 data using MODTRAN fed with the SeeBor V5.0 atmosphere profile data set, and the algorithm's accuracy is better than 0.8 K for all conditions in theory. Sensitivity analysis indicates that the LST error mainly comes from the uncertainty of LSEs and TPW: 1% uncertainty in LSEs will lead to RMSE increment of 0.08∼0.53 K, while an uncertainty of ±0.5 cm in TPW will cause RMSE increased by 0.02 to 0.33 K.

Before LST retrieval, the TIRS bands 10 and 11 were intercalibrated against the IASI/Metop-B hyperspectral channels over the Arctic area, and on average, the calibration biases of the TIRS bands 10 and 11 are −0.54±1.21 K and −1.52±1.35 K, respectively. The GSW algorithm was applied to LST retrieval from re-calibrated and clear sky Landsat-8 data in 2015, in which LSEs in the TIRS bands 10 and 11 were estimated from the OLI data using the NBEM method and TPW was extracted from the temporally and spatially nearest ECMWF reanalysis data. The derived LST was cross-validated with that extracted from the MOD11_L2 V6 product over the Eurasian continent with latitude larger than 50°N and longitude from 20°E to 130°E. In contrast to LSEs extracted in the MOD11_L2 V6 product and TPW extracted from the MOD07_L2 V6 product, the LSEs in the TIRS bands 10 and 11 estimated by the NBEM method are, respectively, 0.016±0.005 and 0.013±0.003 overestimated, whereas the TPW extracted from ECMWF reanalysis data is 0.55±0.26 cm underestimated. The results reveal that the uncertainty in LSEs and TPW has strong impacts on retrieved LST: the LST errors in this work are −1.45±0.80 K and −0.49±0.78 K on average before and after correction of LSEs and TPW. Generally, the development of GSW algorithm is successful and the

derived LST is consistent with the MOD11_L2 V6 LST and the results in previous research.

To improve the accuracy of derived LST, more accurate LSEs and TPW are required. As presented in Section II, almost none of existing LSE estimation methods is suitable for Landsat-8. Another alternative method is to deduce the LSEs from existing LSE product with similar spatial resolution, e.g., the ASTER GED v4 product. However, it is difficult to acquire spatially and temporally matching data between polar-orbiting satellites due to high spatial resolution (narrow swath). For TPW, although it could be corrected with in-situ measurements or third party product, similar problems of spatial and temporal resolutions also exist. It is counting on more infrared channels appeared in next generation of Landsat satellites, and thus both LSEs and TPW can be directly retrieved from satellite measurements. In addition, it is necessary to validate the results in this work with in-situ measurements in larger region and longer period of time.

ACKNOWLEDGMENT

Many thanks are given to the anonymous reviewers for their valuable comments and suggestion.

REFERENCES

[1] P. J. Sellers, F. G. Hall, G. Asrar, D. E. Strebel, and R. E. Murphy, "The first ISLSCP field experiment (FIFE)," *Bull. Amer. Meteorol. Soc.*, vol. 69, pp. 22–27, Jan. 1988.

[2] J. D. Kalma, T. R. McVicar, and M. F. McCabe, "Estimating land surface evaporation: A review of methods using remotely sensed surface temperature data," *Surv. Geophys.*, vol. 29, no. 4, pp. 421–469, Oct. 2008.

[3] B. Tang and Z.-L. Li, "Estimation of instantaneous net surface longwave radiation from MODIS cloud-free data," *Remote Sens. Environ.*, vol. 112, no. 9, pp. 3482–3492, Sep. 2008.

[4] Z.-L. Li *et al.*, "A review of current methodologies for regional evapotranspiration estimation from remotely sensed data," *Sensors*, vol. 9, no. 5, pp. 3801–3853, 2009.

[5] C. Ottlé and D. Vidal-Madjar, "Estimation of land surface temperature with NOAA9 data," *Remote Sens. Environ.*, vol. 40, no. 1, pp. 27–41, 1992.

[6] Z. Qin, A. Karnieli, and P. Berliner, "A mono-window algorithm for retrieving land surface temperature from Landsat TM data and its application to the Israel-Egypt border region," *Int. J. Remote Sens.*, vol. 22, no. 18, pp. 3719–3746, 2012.

[7] L. M. Mcmillin, "Estimation of sea surface temperatures from two infrared window measurements with different absorption," *J. Geophys. Res. Atmos.*, vol. 80, no. 36, pp. 5113–5117, 1975.

[8] F. Becker and Z.-L. Li, "Towards a local split window method over land surfaces," *Int. J. Remote Sens.*, vol. 11, no. 3, pp. 369–393, 1990.

[9] Z. Wan and J. Dozier, "A generalized split-window algorithm for retrieving land-surface temperature from space," *IEEE Trans. Geosci. Remote Sens.*, vol. 34, no. 4, pp. 892–905, Jul. 1996.

[10] Z. Qin, G. Dall'Olmo, A. Karnieli, and P. Berliner, "Derivation of split window algorithm and its sensitivity analysis for retrieving land surface temperature from NOAA-advanced very high resolution radiometer data," *J. Geophys. Res. Atmospheres*, vol. 106, pp. 22655–22670, Oct. 2001.

[11] G.-M. Jiang and Z.-L. Li, "Split-window algorithm for land surface temperature estimation from MSG1-SEVIRI data," *Int. J. Remote Sens.*, vol. 29, no. 20, pp. 6067–6074, 2008.

[12] G.-M. Jiang, W. Zhou, and R. Liu, "Development of split-window algorithm for land surface temperature estimation from the VIRR/FY-3A measurements," *IEEE Geosci. Remote Sens. Lett.*, vol. 10, no. 4, pp. 952–956, Jul. 2013.

[13] G.-M. Jiang and R. Liu, "Retrieval of sea and land surface temperature from SVISSR/FY-2C/D/E measurements," *IEEE Trans. Geosci. Remote Sens.*, vol. 52, no. 10, pp. 6132–6140, Oct. 2014.

[14] G. Sòria and J. A. Sobrino, "ENVISAT/AATSR derived land surface temperature over a heterogeneous region," *Remote Sens. Environ.*, vol. 111, no. 4, pp. 409–422, 2007.

[15] X. Meng, H. Li, Y. Du, Q. Liu, J. Zhu, and L. Sun, "Retrieving land surface temperature from Landsat 8 TIRS data using RTTOV and ASTER GED," in *Proc. Geosci. Remote Sens. Symp.*, Jul. 2016, pp. 4302–4305.

[16] F. Wang, Z. Qin, C. Song, L. Tu, A. Karnieli, and S. Zhao, "An improved mono-window algorithm for land surface temperature retrieval from Landsat 8 thermal infrared sensor data," *Remote Sens.*, vol. 7, no. 4, pp. 4268–4289, 2015.

[17] O. Rozenstein, Z. Qin, Y. Derimian, and A. Karnieli, "Derivation of land surface temperature for Landsat-8 TIRS using a split window algorithm," *Sensors*, vol. 14, no. 4, pp. 5768–5780, 2014.

[18] J. C. Jimenez-Munoz, J. A. Sobrino, D. Skokovic, C. Mattar, and J. Cristobal, "Land surface temperature retrieval methods from Landsat-8 thermal infrared sensor data," *IEEE Geosci. Remote Sens. Lett.*, vol. 11, no. 10, pp. 1840–1843, Oct. 2014.

[19] M. Jin, J. Li, C. Wang, and R. Shang, "A practical split-window algorithm for retrieving land surface temperature from Landsat-8 data and a case study of an urban area in China," *Remote Sens.*, vol. 7, no. 4, pp. 4371–4390, 2015.

[20] T. Song *et al.*, "Comparison of four algorithms to retrieve land surface temperature using Landsat 8 satellite," *J. Remote Sens.*, vol. 19, pp. 1993–2002, May 2015.

[21] A. Berk *et al.*, "MODTRAN cloud and multiple scattering upgrades with application to AVIRIS," *Remote Sens. Environ.*, vol. 65, no. 3, pp. 367–375, 1998.

[22] D. F. Andrews, "A robust method for multiple linear regression," *Technometrics*, vol. 16, no. 4, pp. 523–531, 1974.

[23] J. W. Salisbury and D. M. D'Aria, "Emissivity of terrestrial materials in the 3–5 μm atmospheric window," *Remote Sens. Environ.*, vol. 47, no. 3, pp. 345–361, 1994.

[24] W. C. Snyder, Z. Wan, Y. Zhang, and Y.-Z. Feng, "Classification-based emissivity for land surface temperature measurement from space," *Int. J. Remote Sens.*, vol. 19, no. 14, pp. 2753–2774, 1998.

[25] A. A. Van De Griend and M. Owe, "On the relationship between thermal emissivity and the normalized difference vegetation index for natural surfaces," *Int. J. Remote Sens.*, vol. 14, no. 6, pp. 1119–1131, 1993.

[26] J. A. Sobrino and N. Raissouni, "Toward remote sensing methods for land cover dynamic monitoring: Application to Morocco," *Int. J. Remote Sens.*, vol. 21, no. 2, pp. 353–366, 2000.

[27] J. A. Sobrino *et al.*, "Land surface emissivity retrieval from different VNIR and TIR sensors," *IEEE Trans. Geosci. Remote Sens.*, vol. 46, no. 2, pp. 316–327, Feb. 2008.

[28] J. A. Sobrino, J. C. Jiménez-Muñoz, and L. Paolini, "Land surface temperature retrieval from LANDSAT TM 5," *Remote Sens. Environ.*, vol. 90, no. 4, pp. 434–440, 2004.

[29] F. Becker and Z.-L. Li, "Temperature-independent spectral indices in thermal infrared bands," *Remote Sens. Environ.*, vol. 32, no. 1, pp. 17–33, Apr. 1990.

[30] Z. Wan and Z.-L. Li, "A physics-based algorithm for retrieving land-surface emissivity and temperature from EOS/MODIS data," *IEEE Trans. Geosci. Remote Sens.*, vol. 35, no. 4, pp. 980–996, Jul. 1997.

[31] A. Gillespie *et al.*, "A temperature and emissivity separation algorithm for advanced Spaceborne thermal emission and reflection radiometer (ASTER) images," *IEEE Trans. Geosci. Remote Sens.*, vol. 36, no. 4, pp. 1113–1126, Apr. 1998.

[32] T. N. Carlson and D. A. Ripley, "On the relation between NDVI, fractional vegetation cover, and leaf area index," *Remote Sens. Environ.*, vol. 62, no. 3, pp. 241–252, 1997.

[33] J. A. Sobrino, V. Caselles, and F. Becker, "Significance of the remotely sensed thermal infrared measurements obtained over a citrus orchard," *ISPRS J. Photogramm. Remote Sens.*, vol. 44, no. 6, pp. 343–354, 1990.

[34] A. M. Baldridge, S. J. Hook, C. I. Grove, and G. Rivera, "The ASTER spectral library version 2.0," *Remote Sens. Environ.*, vol. 113, no. 4, pp. 711–715, 2009.

[35] G.-M. Jiang, Z.-L. Li, and F. Nerry, "Land surface emissivity retrieval from combined mid-infrared and thermal infrared data of MSG-SEVIRI," *Remote Sens. Environ.*, vol. 105, no. 4, pp. 326–340, 2006.

[36] J. A. Sobrino *et al.*, "Multi-channel and multi-angle algorithms for estimating sea and land surface temperature with ATSR data," *Int. J. Remote Sens.*, vol. 17, no. 11, pp. 2089–2114, 1996.

[37] Z. Wan, "New refinements and validation of the collection-6 MODIS land-surface temperature/emissivity product," *Remote Sens. Environ.*, vol. 140, pp. 36–45, Jan. 2014.
[38] J. A. Barsi, J. R. Schott, S. J. Hook, N. J. Raqueno, B. L. Markham, and R. G. Radocinski, "Landsat-8 thermal infrared sensor (TIRS) vicarious radiometric calibration," *Remote Sens.*, vol. 6, no. 11, pp. 11607–11626, 2014.
[39] L. Wang *et al.*, "Consistency assessment of Atmospheric Infrared Sounder and Infrared Atmospheric Sounding Interferometer radiances: Double differences versus simultaneous nadir overpasses," *J. Geophys. Res. Atmospheres*, vol. 116, pp. 755–764, Jun. 2011.
[40] M. M. Gunshor, T. J. Schmit, and W. P. Menzel, "Intercalibration of the infrared window and water vapor channels on operational geostationary environmental satellites using a single polar-orbiting satellite," *J. Atmos. Ocean. Technol.*, vol. 21, no. 1, pp. 61–68, 2004.
[41] M. M. Gunshor, T. J. Schmit, W. P. Menzel, and D. Tobin, "Intercalibrating geostationary imagers via polar orbiting high spectral resolution data," *Proc. SPIE*, vol. 6684, p. 66841H, Sep. 2007.
[42] G. M. Jiang, H. Yan, and L. L. Ma, "Intercalibration of SVISSR/FY-2C infrared channels against MODIS/Terra and AIRS/Aqua channels," *IEEE Trans. Geosci. Remote Sens.*, vol. 47, no. 5, pp. 1548–1558, May 2009.
[43] G.-M. Jiang, Z.-Y. Wang, and J. Wang, "Inter-calibration of VIRR/FY-3A/B split-window channels with AIRS/Aqua and IASI/Metop-A measurements," *Int. J. Remote Sens.*, vol. 37, no. 22, pp. 5249–5269, 2016.
[44] G.-M. Jiang, S. Li, and Z.-Y. Wang, "Intercalibration of IRAS/FY-3B infrared channels with IASI/Metop-A 1C data," *IEEE J. Sel. Topics Appl. Earth Observ. Remote Sens.*, vol. 10, no. 6, pp. 2510–2517, Jun. 2017.
[45] Z. Wan, "New refinements and validation of the MODIS land-surface temperature/emissivity products," *Remote Sens. Environ.*, vol. 112, no. 1, pp. 59–74, 2008.
[46] G.-M. Jiang, "Intercalibration of infrared channels of polar-orbiting IRAS/FY-3A with AIRS/Aqua data," *Opt. Exp.*, vol. 18, no. 4, pp. 3358–3363, 2010.
[47] C. Du *et al.*, "A practical split-window algorithm for estimating land surface temperature from Landsat 8 Data," *Remote Sens.*, vol. 7, no. 1, pp. 647–665, 2015.
[48] B. R. Nikam, F. Ibragimov, A. Chouksey, V. Garg, and S. P. Aggarwal, "Retrieval of land surface temperature from Landsat 8 TIRS for the command area of Mula irrigation project," *Environ. Earth Sci.*, vol. 75, p. 1169, Aug. 2016.
[49] Y. Wang, J. Zhou, M. Li, and X. Zhang, "Validation of Landsat-8 TIRS LAND surface temperature retrieved from multiple algorithms in an extremely arid region," in *Proc. Geosci. Remote Sens. Symp.*, 2016, pp. 6934–6937.

SHANSHAN LI received the B.S. degree in electronic science and technology from Sichuan University, Chengdu, China, in 2015. She is currently pursuing the graduate degree in electromagnetic field and microwave technology with Fudan University, Shanghai, China.

Her research interests include inter-calibration and land surface temperature retrieval from satellite data.

GENG-MING JIANG (M'11) received the B.S. degree in photogrammetric engineering and remote sensing from the Wuhan Technical University of Surveying and Mapping, Wuhan, China, in 1997, the M.S. degree in cartography and geographical information system from the Institute of Remote Sensing Applications, Chinese Academy of Sciences, Beijing, China, in 2003, and the Ph.D. degree in remote sensing from the Université Louis Pasteur, Strasbourg, France, in 2007.

Dr. Jiang is currently an Associate Professor with the Key Laboratory for Information Science of Electromagnetic Waves (Ministry of Education), Fudan University, Shanghai, China. His research interests include quantitative remote sensing and digital image processing.